The fast response of tropical cyclones to black carbon

Xin Rong Chua*

Program in Atmospheric and Oceanic Sciences, Princeton University, Princeton, New Jersey, USA

Yi Ming

Geophysical Fluid Dynamics Laboratory/NOAA, Princeton, New Jersey, USA

**Corresponding author address:* Program in Atmospheric and Oceanic Sciences, Princeton University, 300 Forrestal Road, Sayre Hall, Princeton, New Jersey, USA

E-mail: xchua@princeton.edu

ABSTRACT

Using an atmospheric general circulation model capable of simulating tropical cyclones (TCs), we investigate how their frequency and intensity would vary in response to the direct radiative effect of black carbon (BC) on fast time scales. As BC is spatially inhomogenous, sensitivity experiments are conducted to shed light on the relative importance of horizontal and vertical distributions. A 10-fold increase of the present-day BC loadings leads to a 21% decrease in TC frequency. BC over the ocean and land both contribute significantly to the overall reduction. In contrast, the vertical structure of BC plays a crucial role in determining its potency in modifying TCs. Free-tropospheric BC is responsible for most of the reduction in TCs, while its boundary layer counterpart has no appreciable effect. One can relate the reduction in TC frequency to the decrease in tropospheric latent heating (precipitation) and the concurrent weakening of the mid-tropospheric vertical velocity. BC also gives rise to a pronounced decrease in TC intensity. A doubling of CO_2, however, does not show such an effect despite lower TC count. The results are in qualitative agreement with the changes in potential intensity (PI). The BC-induced decrease in PI can be attributed to an increase in 100-hPa (outflow) temperature and a moistening of the boundary layer. The former leads to lower thermodynamic efficiency, and provides an explanation for the decrease in intensity. This suggests that unevenly distributed aerosols may affect extreme weather events through physical mechanisms that are more complex than for well-mixed greenhouse gases.

1. Introduction

Absorbing aerosols, such as black carbon (BC) and dust, can significantly perturb Earth's radiative balance. Strongly absorbing in the shortwave, BC has an estimated global-mean preindustrial-to-present-day top-of-the-atmosphere (TOA) radiative forcing of 0.3-1.1 W m^{-2} (Myhre et al. 2013), the third largest anthropogenic warming effect on climate after carbon dioxide (CO_2) and methane. In contrast to well-mixed greenhouse gases, the radiative effect of BC varies with its highly uneven horizontal and vertical distributions. The spatial inhomogeneity of BC arises from non-uniform surface emissions and short atmospheric residence time (days) (Bond et al. 2013). In particular, the tropics contribute more than half of the global BC emissions (Bond et al. 2013), and the associated radiative effect is amplified by the strong local insolation (Persad et al. 2012). The spatial distribution of dust is also highly variable, with North Africa as one of the major source regions (Ginoux et al. 2012). Its radiative effect is dependent on complex mineral compositions and optical properties, which give rise to a wide range of combinations in terms of the relative importance of absorption versus scattering, both in the shortwave and in the longwave. In a global model simulation using the optical characteristics of absorbing dust over the southwestern Sahara, Strong et al. (2015) found that dust enhanced the regional net TOA clear-sky shortwave absorption by up to 30 W m^{-2}, while reducing the surface shortwave fluxes by a similar magnitude. Besides the direct effect, absorbing aerosols are also capable of indirectly modifying the global radiative balance through increasing cloud albedo (Twomey 1974) and lifetime (Albrecht 1989) – collectively known as the indirect effects. Since the indirect effects still suffer from large uncertainties (e.g. Carslaw et al. 2013), this study will focus on the climate response to the direct effect in isolation.

Once being subjected to the radiative perturbation of absorbing aerosols, the atmosphere, land and ocean components of the climate system must adjust collectively to re-establish the TOA radiative balance on the planetary scale. As the atmosphere and land respond on much shorter time scales (days to months) than the ocean (years and longer), there is value in establishing a holistic understanding of the climate impacts of absorbing aerosols by separately investigating the fast and slow responses (e.g. Andrews et al. 2010). The focus of this work is on the fast response of the tropical atmosphere-land system from the perspective of tropical cyclones (TCs). Given that extreme weather events such as TCs are under heavy influence of large-scale environment, we begin by reviewing the current literature on the impacts of absorbing aerosols on the tropical general circulation and precipitation.

Absorbing aerosols increase the shortwave radiation retained within the atmosphere. On fast time scales, the atmospheric energy balance dictates that the increased absorption must be balanced, to first order, by a reduction in the tropical-mean latent heat release by precipitation (Andrews et al. 2010; Ming et al. 2010). One can decompose the fractional change in precipitation into those in convective mass flux and in boundary layer specific humidity (Held and Soden 2006). Since the latter is small under fixed sea surface temperatures (SST) (as is the case for the fast response), the reduction of tropical-mean precipitation can be linked to a decrease in convective mass flux, which is concurrent with a weakening of the tropical general circulation in climate model simulations (Held and Soden 2006; Ming and Ramaswamy 2011).

The radiative heating from absorbing aerosols can influence different monsoonal systems. In the atmosphere-land-only context, Miller and Tegen (1998) discussed an increase in the the West African JJA monsoon precipitation in response to the heating, but Mahajan et al. (2012) later found a decrease in precipitation over the same region [see Table 1 of Strong et al. (2015) for a quantitative comparison]. For Asia, where the emissions of BC are concentrated, climate models are in qualitative agreement on the direct effect of absorbing aerosols on fast time scales. Absorbing aerosols are thought to increase pre-monsoonal and decrease monsoonal rainfall over India (Chung et al. 2002; Collier and Zhang 2009; Mahmood and Li 2013), while suppressing summer monsoonal rainfall over South China (Persad et al. 2017). To explain features of the induced monsoonal changes over India and China, it was first proposed that absorbing aerosols would generally lead to ascending motion, which tends to enhance precipitation (Menon et al. 2002). To further address the shift of the timing of the Indian monsoon, Lau et al. (2006) suggested that pre-monsoonal aerosol heating strengthened the meridional tropospheric temperature gradient that drives the monsoon. Bollasina et al. (2008) postulated that this enhanced temperature gradient could also be due to the observed reduction in cloud cover in May, possibly due to aerosol heating, which increases the amount of shortwave radiation able to reach and warm the surface. To disentangle the combined effects of atmospheric heating and surface dimming, Persad et al. (2017) systematically considered the impacts of idealized atmospheric heating and surface dimming on moisture convergence and evaporation. They found that the sign of the aerosol-induced precipitation response over China (a net reduction) was the same as that of the response to the imposed surface dimming, as opposed to the atmospheric heating. While atmospheric heating did not determine the sign of precipitation change, it was crucial for differentiating the hydroclimate impacts of absorbing versus scattering aerosols. On the whole, existing works substantiated the potent influence of BC on large-scale circulation and precipitation. One should be cautious in generalizing the findings on mean precipitation to extreme precipitation. The tropical-mean and continental-scale monsoonal precipitation changes caused by absorbing aerosols concern averaging over large domains and long durations. In comparison, extreme precipitation is a subset of the total precipitation corresponding to high percentiles of the intensity distribution, or weather events such as TCs. One cannot rule out a re-distribution of precipitation of different intensities while the average conforms to the large-scale constraints that have been identified. On the other hand, it is well-known that certain large-scale conditions exert strong controls over the development of weather events, a classical example being that low vertical wind shear and high mid-tropospheric humidity have to be satisfied for TCs to occur (e.g. Gray 1998). In this sense, the past work on aerosol-induced large-scale circulation changes provides a useful starting point for thinking about possible changes in the frequency and intensity of extreme precipitation.

Most of the published literature on the fast TC response to BC focused on environmental factors such as the strength of convection, sources of vorticity disturbances (e.g. African easterly waves) and wind shear. Using satellite observations of the Saharan Air Layer, Dunion and Velden (2004) suggested that dust reinforced a temperature inversion, which might suppress convection, easterly waves, and hence TC activity. Subsequent cloud-resolving model (CRM) case studies of TCs supported the idea that atmospheric heating could reduce TC activity. One such study based on background conditions similar to Hurricane Katrina found lower TC wind speeds when a partially absorbing aerosol was added, as opposed to a purely scattering aerosol (Wang et al. 2014). Using CRM simulations of the Atlantic TC development region in June 2006, Chen et al. (2016) found a strengthening of convection by high-altitude dust and a weakening of convection by low-altitude dust. In a TC forecast run, the increased convective inhibition coincided with lower TC wind speeds. The effect of dust on African easterly waves, however, remains elusive. With the help of an analytic expression for the wave response, Grogan et al. (2016) suggested that the different spatial gradients of dust used in previous studies might partially explain the disagreement in the sign of the dust impacts on easterly wave activities. Spatial variations also seem to be crucial for understanding the impacts related to circulation changes, with model results showing shifts (Bretl et al. 2015) or intensification (Evan et al. 2011) of TCs depending on the TC development region considered. As almost all prior studies focused on individual storms, basins or seasons, the question of how absorbing aerosols affect TC frequency and intensity statistics across all basins still remains to be addressed. That the current-generation high-resolution atmospheric general circulation models (AGCMs) are able to resolve global TC climatology (Murakami et al. 2012; Walsh et al. 2015) affords us an opportunity to shed some light on the question.

Such AGCMs have already been utilized to study TC changes under global warming. A prominent example is the Geophysical Fluid Dynamics Laboratory (GFDL) High-Resolution Atmospheric Model (HiRAM), which was employed to simulate the fast response in TC frequency (number count) and intensity (maximum wind speed) to a doubling of CO_2 (Held and Zhao 2011, henceforth HZ11). HZ11 found that TC frequency decreased significantly, confirming the earlier results of Yoshimura and Sugi (2005), while TC intensity decreased only slightly. Both HZ11 and Sugi et al. (2012) made scaling arguments connecting changes in TC frequency to large-scale vertical velocity, suggesting that the latter is a better predictor of TC frequency changes than wind shear or potential intensity (PI) (Emanuel 1986). Following the experimental design of HZ11, Walsh et al. (2015) reproduced the decreases in TC frequency and genesis-weighted vertical velocity in response to CO_2 with a suite of global models. While these global model simulations have advanced our understanding of the fast response to well-mixed greenhouse gases, they do not address, at least directly, the impacts arising from the horizontal and vertical inhomogeneity of aerosol forcings.

This work uses HiRAM to investigate the fast response of simulated TCs to changes in BC loadings as well as horizontal and vertical distributions. Section 2 covers some key features of HiRAM and the experimental design. In Section 3, we describe the direct radiative heating of BC in different cases, the resulting changes in TC frequency (in relation to mid-tropospheric vertical velocity) and in TC intensity (as viewed from the perspective of PI). A discussion of the implications and limitations is given in Section 4, and a summary of the key findings in Section 5.

2. Methodology

a. Model Description

The GFDL HiRAM (Zhao et al. 2009, 2012) uses a finite-volume cubed-sphere dynamical core (Putman and Lin 2007) with 180 grid points on each side, yielding a horizontal resolution of approximately 50 km, and 32 vertical levels. Most of the physics parameterizations in HiRAM follow those of the GFDL AM2.1 (GFDL Atmospheric Model Development Team 2004). The exceptions are the shallow convection scheme (Bretherton et al. 2004), the diagnostic cloud fraction scheme (Zhao et al. 2009), and the land model (Dunne et al. 2012). The choice of convection scheme results in a significant portion of convection in HiRAM being resolved at the grid scale, as opposed to being parameterized. The large-scale fraction of the tropical precipitation is 39% for HiRAM, as compared to 7.5% for AM2.1 (with a horizontal resolution of $\sim$200 km). The simulated TC genesis climatology, including spatial distribution and seasonal cycles, agrees well with observations (Zhao et al. 2009). Similar to other global models, HiRAM underestimates TC intensity (Shaevitz et al. 2014). The detection algorithm used in this study defines TC as a sustained warm-core vortex with 10-meter winds exceeding 15.3 m s^{-1} (Zhao et al. 2009, 2012). The algorithm occasionally identifies storms more than 30° from the equator as TCs, which are excluded from this analysis.

The offline present-day (1980-1999) aerosol climatology used in HiRAM is generated with a chemical transport model (Model for Ozone and Related Chemical Tracers, MOZART) (Horowitz et al. 2003; Horowitz 2006), and does not interact with HiRAM's meteorology. The optical properties of aerosols are calculated with the Mie theory. In particular, BC is assumed to follow a log-normal distribution (with a geometric mean radius of 0.0118 μm and a geometric standard deviation of 2.0) and have a single-scatter albedo of $<$0.35 in the visible spectrum (Haywood and

Ramaswamy 1998). Aerosol indirect effects are not included, as cloud droplet number concentrations are fixed at 150 cm^{-3} over the land and 50 cm^{-3} over the ocean.

b. Experimental design

We explore the fast TC response to BC across a wide range of spatial distributions in a series of model simulations. The control experiment (CNTL) uses the present-day aerosol climatology as described above. The BC loadings are increased uniformly by ten times in the 10X experiment. The magnitude of the perturbation is motivated partly by the well-documented underestimation of BC concentrations in global models (Bond et al. 2013; Cohen and Wang 2014), and the desire to achieve a favorable signal-to-noise ratio. Due to similar considerations, recent studies of BC impacts on hydroclimate chose comparable, or even larger increases (Sand et al. 2015; Guo et al. 2016; Kovilakam and Mahajan 2016). We consider BC increases isolated over the land (LAND) and over the ocean (OCEAN) separately. To investigate the sensitivity of TCs to the vertical distribution of BC, we confine BC increases to the free troposphere ($\sigma < 0.78$, roughly above 780 hPa) and to the boundary layer ($\sigma \geq 0.78$, roughly below 780 hPa) in the FT and BL experiments, respectively. Similar to HZ11, we double CO_2 from its present-day value in the CO2 experiment. All experiments are run from 1980 to 1999 using SSTs and sea ice prescribed from the Hadley Centre Sea Ice and Sea Surface Temperature (HADISST) observational data set (Rayner et al. 2003). The first year is discarded as spinup, and the remaining 19 years are analyzed.

3. Results

a. Magnitudes and spatial distributions of atmospheric absorption

We use the tropical-mean changes in atmospheric absorption as a starting point for understanding the basic characteristics of the fast response to increased BC and CO_2 (Table 1). The shortwave absorption (AS) is computed as the net shortwave (SW) radiative fluxes entering the atmospheric column from the TOA and surface (SFC), i.e. $AS = SW_{\downarrow}^{TOA} - SW_{\uparrow}^{TOA} + SW_{\uparrow}^{SFC} - SW_{\downarrow}^{SFC}$, where the subscripts $\uparrow$ and $\downarrow$ denote upward and downward fluxes, respectively, and positive values of AS represent net atmospheric heating. Similarly, the longwave absorption (AL) can be calculated as $LW_{\uparrow}^{SFC} - LW_{\downarrow}^{SFC} - OLR$, where OLR is the TOA outgoing longwave radiation. The increase in shortwave absorption (δAS) amounts to 9.9 W m^{-2} in the 10X case. Fortuitously, the LAND (4.6 W m^{-2}) and OCEAN (5.2 W m^{-2}) cases each account for about half of the increase in 10X. The FT (5.2 W m^{-2}) and BL (5.0 W m^{-2}) cases also contribute roughly equally. Hence there is no need for normalization when comparing the two pairs of experiments. In comparison, the CO_2 forcing mostly manifests as an increase of longwave absorption (2.3 W m^{-2}).

The geographical distributions of δAS due to the BC perturbations are given in Figure 1. The pattern in the 10X case reflects the present-day BC climatology. The largest increases are found over the main source regions, namely South and East Asia, Central Africa and the Amazon, where the local values can exceed the tropical-mean by a factor of more than three. Since TC genesis take place exclusively over the ocean, one may speculate that the efficacy of BC-induced absorption in altering TC would depend on whether it is over the land or over the ocean. To facilitate this discussion, we calculate the fraction of the increased absorption over the ocean (f_o) as $a_o \delta AS_o / \delta AS$, where a_o is the fraction of the tropics covered by the ocean (0.75), and AS_o is the increase in shortwave absorption averaged over the ocean. As a limiting case, a f_o of one means that all the increased absorption occurs over the ocean. Despite stronger absorption over the land than over the ocean, f_o is 0.55 in 10X due to much larger oceanic coverage. As expected, f_o is effectively zero in LAND and one in OCEAN. That f_o is larger in the FT case (0.62) than in the BL case (0.48) indicates that BC is more elevated over the ocean, consistent with free-tropospheric transport from land source regions to adjacent oceans.

The vertical distributions of the tropical-mean shortwave heating rate changes are shown in Figure 2. The profile of the 10X case is bottom-heavy, with a maximum of 0.17 K day^{-1} at $\sim$850 hPa, representing a 17% increase over the control value. The heating decreases gradually above 850 hPa: the heating rate increase at 500 hPa is about 45% of that at 850 hPa. As explained above, the heating profile is indeed more bottom-heavy in LAND than in OCEAN. This is particularly true above $\sim$150 hPa, where the heating rate in OCEAN more than doubles that in LAND. This has important implications for TC responses, a point to which we will return later. Only the free-tropospheric and (boundary layer) heating is present in the FT (BL) case. The longwave heating in the CO2 case is mostly confined between 600 and 850 hPa.

b. Changes in TC frequency and intensity

Except for BL, all perturbation cases show statistically significant decreases in TC frequency (Table 2). The tropical-mean reduction is 21% in the 10X case. Despite similar increases in shortwave absorption, the reduction in LAND (8.4%) is considerably less than in OCEAN (13%), meaning that BC over the land is not as effective at changing TCs as that over the ocean. Although this is hardly surprising given that TC genesis occurs exclusively over the ocean, the extent to which land-based atmospheric absorption can affect TC speaks to the tightly coupled nature of the tropical circulation due to the lack of scale separation. It is also interesting to note that the combined effects, if assumed to be linear, are virtually the same as the 10X case. TC formation is very sensitive to the vertical structure of atmospheric absorption. The reduction amounts to 14% in the FT case, while BL yields no significant change. They do not add up linearly to the 10X case. This suggests that free-tropospheric absorption is substantially more effective at suppressing TCs than the same magnitude of absorption placed within the boundary layer. Hurricanes (with maximum wind speeds greater than 29.5 m s^{-1}) decrease at rates even higher than TC for all BC cases, hinting at possible influence on intensity. This, however, does not hold for CO2. In terms of hemispheric responses, the fractional changes in the Northern Hemisphere are usually greater (less negative) than in the Southern Hemisphere, which is even the case for CO2. This is contrary to the doubling CO_2 simulation in HZ11, and suggests that longer integrations are needed for assessing the robustness of any disparity between the hemispheres.

The geographical distributions of the changes in annual-mean TC genesis counts are shown in Figure 3. The decreases in 10X are distributed unevenly among the oceanic basins, concentrated over the main development regions with West Pacific being the most prominent one, while no robust signal emerges on their poleward flanks. The same is true to the other cases, with BL as a notable exception.

Following HZ11, one can write the number of TCs with the maximum lifetime wind speed exceeding a given value I ($F(I)$) as $NP(I)$, where N is the total number of TCs, and $P(I)$ the normalized cumulative probability distribution of TC intensity. Then the change $\delta F(I)$ can be decomposed into two parts: $\delta NP(I)$ and $N\delta P(I)$. The $\delta NP(I)$ term represents the change in TC intensity distribution solely due to the change in the overall TC frequency discussed above. The $N\delta P$ term arises from a change in the normalized intensity distribution. δF and $N\delta P$ are plotted in the upper and middle panels of Figure 4, respectively. For 10X, F decreases at all intensity levels. The same is apparently true for CO2. The major difference is that increased BC causes a weakening of TC intensity (as measured by I) as one can gather from the substantial reductions from $N\delta P$, while CO_2 does not alter TC intensity appreciably. The weakening is present in other BC cases, albeit to a lesser extent than 10X.

It is more natural to quantify changes in TC intensity in terms of maximum wind speed. To that end, one can plot the change in wind speed (δI) for each percentile bin, which is labeled with the corresponding wind speed in CNTL (the lower panel of Figure 4). The δI result confirms the widespread weakening of intensity inferred from $N\delta P$ for BC cases.

c. Connections with large-scale environment

It is well known that increased atmospheric absorption, whether it is due to absorbing aerosols or CO_2, would lower latent heating or precipitation as part of the fast response (Andrews et al. 2010; Ming et al. 2010). This is borne out in Table 1. For 10X, the tropical-mean latent heating (δLH) decreases by 4.2 W m^{-2}, less than half of the imposed BC heating (9.9 W m^{-2}). A reduction in sensible heating (δSH, 2.5 W m^{-2}) accounts for part of the difference. The ratio of δSH to δLH (analogous to the canonical Bowen's ratio) is 0.6. The precipitation reduces by 4.5%. Although δSH and δLH are negative for all other BC cases, their relative magnitude varies with spatial distribution. The ratio is substantially larger for LAND (1.4) than for OCEAN (0.26). This is because moisture is of limited supply over the land, making it possible for sensible heating to dominate latent heating. A different mechanism is behind the divergence between FT (0.35) and BL (0.90) in this regard. Originating at the surface and permeating the boundary layer by small-scale eddies, sensible heating is more effective at balancing out BC heating placed in the boundary layer. Adjusting moist convection and associated latent heating, on the other hand, is the main means to counteract free-tropospheric heating. CO_2 is more potent than BC in altering latent heating to the extent that the decrease in latent heating (2.4 W m^{-2}) is even slightly more than the longwave heating (2.3 W m^{-2}).

Although the fractional reductions in latent heating (precipitation) are much smaller than those in TC count, they are positively correlated. A linear regression through the origin (used throughout the paper) yields a correlation coefficient (R) of 0.75, with BL as an outlier. This hints at possible connection between TC frequency and tropical-mean precipitation, a quantity under strong energetic constraints.

To move beyond tropical means and focus on TC genesis seasons and regions, the monthly-mean spatial pattern of genesis [$G(x,y,t)$,t=1,...,12] can be used for computing the weighted mean of a variable $A(x,y,t)$ ($[A]_G$) as $\overline{G(x,y,t)A(x,y,t)}/\overline{G(x,y,t)}$, and the weighted spatial pattern ($[A(x,y)]_G$) as $\widetilde{G(x,y,t)A(x,y,t)}/\widetilde{G(x,y,t)}$, where the overline denotes time and spatial averaging and the tilde time averaging. The fractional changes in genesis-weighted precipitation ($\delta[P]_G$), along with a few other important variables, are listed in Table 3. $\delta[P]_G$ are highly correlated (R = 0.81) with those of the un-weighted tropical-mean δP across all cases, but are three times as large. As such, $\delta[P]_G$ is much closer to, albeit consistently smaller than, the variations in TC frequency than δP in terms of fractional changes.

The genesis-weighted 500-hPa vertical velocity ($[-\omega_{500}]_G$) filters out subsidence regions, and decreases in all cases (Table 3). The magnitudes are consistently larger than $\delta[P]_G$. A linear regression against the variations in total TC count yields a slope of 1.0 and a R of 0.85, making $\delta[-\omega_{500}]_G$ a better predictor of TC frequency changes than $\delta[P]_G$. This suggests that TC frequency is proportional to the total amount of deep convection over the genesis regions as the latter plays an important role in moistening the mid-troposphere, a condition essential for genesis (HZ11). Note that the fractional contribution of TCs to precipitation (and therefore vertical velocity) is small in HiRAM (HZ11). The spatial patterns of $[-\omega_{500}]_G$ is shown in Figure 5. The reduction is robust over the main development regions, and is not as noisy as TC counts (Figure 3). There is no apparent difference among the experiments including CO2.

The vertical shear index (S) is computed as the absolute value of the difference between monthly-mean 850 and 200-hPa vector winds. The genesis-weighted value increases in all cases (Table 3), which is consistent with lower TC number as it is well known that strong wind shear disfavors genesis. BL is still a notable exception. The correlation coefficient (R) is 0.80. The geographical distributions (Figure 6) appear to be more variable than $[-\omega_{500}]_G$, but rather similar among all the cases.

The potential intensity (PI) theory posits that the maximum wind speed achieved by a TC occurs when the main sources in the entropy budget are the dissipation of kinetic energy and the surface enthalpy flux (e.g. Emanuel 1988; Bister and Emanuel 1998). Furthermore, PI is also thought to be relevant for genesis (Camargo et al. 2007). One can write PI ($\mathscr{I}$) as:

$$\mathscr{I}^2 = \frac{C_k}{C_d}\mathscr{T}\mathscr{E}, \tag{1}$$

where C_k and C_d are the exchange coefficients for enthalpy and momentum, respectively. The term $\mathscr{T}$ is defined as $(T_s - T_o)/T_o$, where T_s and T_o are the surface and outflow temperatures, respectively, and can be perceived as the thermodynamic efficiency of TC. The term $\mathscr{E}$ is the enthalpy difference between the surface and boundary layer, i.e. $c_p(T_s - T_b) + L(q_s^* - q_b)$, where c_p is the specific heat of dry air at constant pressure, L the latent heat of vaporization, q specific humidity and q^* saturation specific humidity. The subscripts s and b denote the surface and boundary layer, respectively. We use a parcel lifting algorithm (Bister and Emanuel 2002) (available at `ftp://texmex.mit.edu/pub/emanuel/TCMAX/`) to estimate the changes in the outflow temperature and enthalpy [see Garner (2015) for detailed discussion]. The resulting changes in genesis-weighted PI are given in Table 3. The variable decreases in all BC cases as well as CO2, in qualitative agreement with lower TC counts. More quantitatively, Camargo et al. (2007) assumed that genesis frequency is proportional to PI raised to the third power, which implies that the fractional change in TC frequency would be three times of that in PI. In this set of simulations, the correlation between the two quantities is exceptionally high ($R = 0.96$). This is mainly because $\delta[\mathscr{I}]_G$ captures the lack of frequency change in the BL case much better than the other three metrics discussed above. Yet, their ratio is about six, suggesting that PI has an even stronger bearing on TC number than suggested by Camargo et al. (2007). Although lower PI is generally consistent with the weakening of TC intensity in BC cases, the reduced PI in CO2 appears to be at odds with unchanged intensity. This issue can be illustrated by contrasting CO2 with LAND. Despite similar $\delta[\mathscr{I}]_G$ in the two cases, LAND shows a distinct decrease in intensity (Figure 4). Figure 7 shows the spatial structures of $\delta[\mathscr{I}]_G$. The decrease is widespread, and relatively uniform over the main development regions. There is no obvious dependence on the spatial distributions of BC or CO_2 forcings.

To better delineate how atmospheric heating alters PI, we decompose it into two components, similar to Gilford et al. (2017). C_k/C_d is constant across our experiments because it is set to be consistent with the dissipative heating in HiRAM (Zhao et al. 2009). Thus the fractional change in PI can be written as:

$$\frac{\delta\mathscr{I}}{\mathscr{I}} = \frac{\delta\mathscr{T}}{2\mathscr{T}} + \frac{\delta\mathscr{E}}{2\mathscr{E}}. \tag{2}$$

It is clear from Table 3 that this linear decomposition holds reasonably well for all cases. The enthalpy difference term ($\delta\mathscr{E}$) roughly tracks the tropical-mean change in latent heating (Table 1), implying that genesis weighting favors latent heat more than sensible heat. This is understandable as TC genesis occurs over the oceanic regions of deep convection where moisture is in abundant supply. As explained above, the atmospheric energy balance dictates that imposed absorption, no matter where it is placed, would reduce the total surface flux, an effect manifested as decreases in $\mathscr{E}$ across all cases.

The thermodynamic efficiency term ($\delta\mathscr{T}$) is more variable than $\delta\mathscr{E}$. BL stands out as the only BC case in which it is substantially smaller than (about one quarter of) the corresponding enthalpy difference term. The same is also true for CO2. The two terms are within a factor of two for other cases. The setup of fixed surface temperature (T_s) means that any change in $\mathscr{T}$ is caused by different outflow temperature (T_o). In the simulations discussed here, genesis-weighted T_o closely tracks (r = 0.99) the average temperature at $\sim$100 hPa, where the thermal inversion marks the tropopause. Thus it is reasonable to think of the decrease in $\mathscr{T}$ as a consequence of the warming at 100 hPa, as opposed to a change of the outflow level. The vertical distributions of the tropical-mean changes in air temperature are plotted in Figure 8. In response to forced radiative heating (Figure 2), the troposphere undergoes modest warming, which is typically confined to be less than 0.5 K below 200 hPa by fixed surface temperature and moist adiabat. The surface control starts to loosen as one moves above 200 hPa (Lin et al. 2017). Strong warming is present in all non-BL cases, reaching about 1.4 K at 100 hPa in 10X and FT. The upper-tropospheric response is rather muted in BL. The warming caused by doubling CO_2 (about 0.5 K at 100 hPa) is in line with what Lin et al. (2017) found with a different GFDL model. These results can explain why atmospheric heating, when located in the free troposphere, causes the thermodynamic efficiency term to decrease.

The strong dependence of the TC response on the vertical structure of imposed absorption motivates us to examine the energy balance within the atmosphere's interior for the FT and BL cases (Figure 9). At each level, the BC-induced shortwave absorption increase must be compensated by changes in longwave radiation, latent heating from the model's convection parameterization and large-scale cloud scheme, and sensible heating from sub-grid vertical diffusion and grid-scale dynamical advection. Note that the vertically-integrated advection term is practically zero, suggesting negligible change in atmospheric energy transport out of the tropics under fixed SST (Held 2001).

For the FT case, the additional shortwave heating is balanced primarily through reducing convective and large-scale latent heating in the lower and mid-troposphere, the root cause of suppressed precipitation. Radiative to first order, the upper-tropospheric energy balance (above $\sim$100 hPa) is re-established by enhancing longwave cooling, which is realized through localized warming. In contrast, the reduction in sensible heating plays a leading role in counteracting boundary layer heating, while convective heating also decreases. These adjustments take place almost entirely within the boundary layer, and the upper troposphere is unchanged.

The PI decomposition also provides important insights into why BC over the ocean is more effective than that over the land in altering TCs. The tropical-mean contribution from latent heating in OCEAN is more than twice of that in LAND (Table 1) due to the abundance of moisture over the ocean. The role of latent heating is further amplified by genesis weighting, which favors the moist deep tropics over the dry subtropics. As a result, the decrease in the enthalpy difference term ($\delta\mathscr{E}$) in OCEAN is more than three times of that in LAND (Table 3). From the perspective of thermodynamic efficiency ($\delta\mathscr{T}$), the tropical-mean 100-hPa or outflow temperature (T_o) increase in OCEAN is about twice of that in LAND (Figure 8), approximately proportional to the shortwave heating rate (Figure 2). This is attributed to oceanic BC being more elevated, and gravity waves being effective at propagating temperature anomaly throughout the tropical free troposphere (Sobel et al. 2001).

4. Discussion

Although the initial perturbation by BC is entirely in the shortwave, the subsequent fast adjustment gives rise to a substantial reduction in longwave absorption (Table 1). In the 10X case, the magnitude of the latter is about 30% of the shortwave absorption. If one thinks of the longwave absorption as the divergence between surface and TOA fluxes, about half of δAL can be attributed to increased OLR, and the other half to decreased net surface longwave flux into the atmosphere. Both are linked partly to atmospheric warming. The clear- and cloud-sky components of δAL have similar magnitudes, and more interestingly, the latter takes place almost entirely over the ocean, which is even the case for LAND, indicating that BC tends to decrease high cloud cover (and thus increase OLR). The high cloud change can be ascribed to suppressed precipitation as high cloud cover and the associated longwave cloud radiative effect (CRE) are known to be tightly coupled to precipitation, both in models and in observations (Hill et al. 2018). Note that CO_2 leads to an increase in shortwave absorption, which is coincidentally also 30% of the imposed longwave absorption (Table 1). This exclusively clear-sky effect suggests that higher water vapor concentrations may be the cause. Further effort is needed to understand why there is no change in CRE given the decreased precipitation.

The atmospheric energy balance argument does not distinguish shortwave and longwave absorption, and what matters is the combined effect. Our results confirm that the downstream impacts on precipitation and TC activities are indeed approximately proportional to the total (shortwave plus longwave) absorption. In this sense, the aforementioned fast adjustment has a tendency to dampen the effect of BC, but enhance the effect of CO_2. This insight helps understand a key finding by Emanuel and Sobel (2013). In that study, the authors conducted a series of radiative-convective equilibrium simulations with a single column model, and showed that precipitation and PI are less sensitive to SST in CO_2 warming experiments than in prescribed SST experiments. We argue that the disparity can be thought of as a manifestation of the fast response to CO_2-induced absorption. Specifically, at $\sim$32X CO_2 ($\sim$37°C), the difference from 1X CO_2 with a prescribed SST of $\sim$37°C amounts to about 0.8 mm day^{-1} (or 23 W m^{-2}) in precipitation. Our work based on a GCM suggests a reduction in precipitation of 2.4 W m^{-2} per doubling of CO_2 or 12 W m^{-2} for 32X. Given how vastly different the two models are, it is encouraging to see that the simulated (inferred) fast responses to CO_2 agree with each other within a factor of 2.

In addition to the shared pathway of curtailing surface enthalpy supply, BC is more effective than CO_2 at altering the upper-tropospheric temperature and thus thermodynamic efficiency. This motivates us to conduct an experiment in which only BC above 200 hPa is increased by 10 times. The resulting warming is confined locally with a magnitude comparable to 10X, while the surface enthalpy does not change. The fractional change of $\mathscr{E}$ is -1.7%, similar to what is in FT (-2.1%). While there is no statistically significant change in TC frequency in this experiment, the reduction in intensity is comparable to FT, especially for winds stronger than 35 m s^{-1}. Taken together, our results suggest that the thermodynamic efficiency term is more important than the enthalpy difference term in affecting TC intensity.

Although it is fully possible that the offline aerosol climatology used in HiRAM may overestimate the amount of upper-tropospheric BC (Koch et al. 2009), there are observational evidences suggesting that aerosols and their precursors can be transported to the upper troposphere and lower stratosphere by deep convection associated with Asian summer monsoon (Yu et al. 2017). Our work shows that the upper-tropospheric temperature is susceptible to even a small radiative perturbation, and the influence of regional aerosols can be felt throughout the tropics. Therefore, the elevated aerosols may have an important effect on TC formation even when they are relatively removed from the main development regions.

BC can potentially affect TCs through cloud microphysics, or the indirect effects. Although cloud processes (such as latent heat release and re-evaporative cooling) are central to TC dynamics, the indirect effects do not alter the atmospheric energetics or thermal structure directly. So, many of the intuitions developed here for radiative perturbations may not be applicable to microphysical perturbations. Unfortunately, we cannot pursue this line of investigation as HiRAM does not consider the indirect effects.

5. Conclusions

This work addresses the direct radiative effect of BC on TC frequency and intensity with an atmospheric model capable of simulating a realistic TC climatology. We consider the impacts of a tenfold increase in BC as compared to CO_2 doubling, focusing on the differences that arise due to the magnitude and distribution of BC perturbations.

There are statistically significant decreases in TC frequency in all the BC cases with free-tropospheric perturbations, even when BC is placed solely over the land. In contrast, the boundary layer BC in isolation does not have an appreciable effect. The lowering of TC frequency correlate well with the reductions in convective activities, as measured by genesis-weighted precipitation and mid-tropospheric ascent. The latter is attributed to added free-tropospheric heating cutting down the need for latent heating. The boundary layer heating, on the other hand, is mostly communicated downward toward the surface by adjusting sensible heating.

As a characteristic difference between the two forcings, BC causes TC intensity to decrease substantively, while CO_2 does not. This cannot be explained by PI, as it shows similar decreases in response to both forcings. An inspection of the thermodynamic efficiency term of PI indicates that BC, when placed in the upper troposphere, can induce significant warming locally, and thus lower the thermodynamic efficiency in a way that uniformly distributed CO_2 cannot. The results suggest that thermodynamic efficiency may be particularly relevant to understanding TC intensity changes.

Acknowledgments. We thank Jenny Chang, Spencer Clark, Stephen Garner, and Ming Zhao for helpful discussion. Ming Zhao shared some of the code used in HZ11 which is used in the analysis in this paper. Nadir Jeevanjee and David Paynter provided constructive internal reviews. The model simulations are archived at GFDL and are available upon request. Xin Rong Chua acknowledges funding from the Singapore National Research Foundation and the Cooperative Institute for Modeling Earth Systems.

References

Albrecht, B. A., 1989: Aerosols, cloud microphysics, and fractional cloudiness. *Science*, **245 (4923)**, 1227.

Andrews, T., P. M. Forster, O. Boucher, N. Bellouin, and A. Jones, 2010: Precipitation, radiative forcing and global temperature change. *Geophys. Res. Lett.*, **37 (14)**.

Bister, M., and K. A. Emanuel, 1998: Dissipative heating and hurricane intensity. *Meteor. Atmos. Phys.*, **65 (3)**, 233–240.

Bister, M., and K. A. Emanuel, 2002: Low frequency variability of tropical cyclone potential intensity 1. Interannual to interdecadal variability. *J. Geophys. Res.-Atmos.*, **107 (D24)**.

Bollasina, M., S. Nigam, and K. Lau, 2008: Absorbing aerosols and summer monsoon evolution over South Asia: An observational portrayal. *J. Climate*, **21 (13)**, 3221–3239.

Bond, T. C., and Coauthors, 2013: Bounding the role of black carbon in the climate system: A scientific assessment. *J. Geophys. Res.-Atmos.*, **118 (11)**, 5380–5552.

Bretherton, C. S., J. R. McCaa, and H. Grenier, 2004: A new parameterization for shallow cumulus convection and its application to marine subtropical cloud-topped boundary layers. Part I: Description and 1D results. *Mon. Wea. Rev.*, **132 (4)**, 864–882.

Bretl, S., P. Reutter, C. C. Raible, S. Ferrachat, C. S. Poberaj, L. E. Revell, and U. Lohmann, 2015: The influence of absorbed solar radiation by Saharan dust on hurricane genesis. *J. Geophys. Res.-Atmos.*, **120 (5)**, 1902–1917.

Camargo, S., A. Sobel, A. G. Barnston, and K. Emanuel, 2007: Tropical cyclone genesis potential index in climate models. *Tellus*, **59A**, 428–443.

Carslaw, K., and Coauthors, 2013: Large contribution of natural aerosols to uncertainty in indirect forcing. *Nature*, **503 (7474)**, 67–71.

Chen, D., Z. Liu, C. Davis, and Y. Gu, 2016: Dust Radiative Effects on Atmospheric Thermodynamics and Tropical Cyclogenesis over the Atlantic Ocean Using WRF-Chem Coupled with an AOD Data Assimilation System. *Atmos. Chem. Phys. Discuss.*, **2016**, 1–29, doi: 10.5194/acp-2016-744.

Chung, C. E., V. Ramanathan, and J. T. Kiehl, 2002: Effects of the South Asian absorbing haze on the northeast monsoon and surface–air heat exchange. *J. Climate*, **15 (17)**, 2462–2476.

Cohen, J. B., and C. Wang, 2014: Estimating global black carbon emissions using a top-down Kalman Filter approach. *J. Geophys. Res.-Atmos.*, **119 (1)**, 307–323.

Collier, J. C., and G. J. Zhang, 2009: Aerosol direct forcing of the summer Indian monsoon as simulated by the NCAR CAM3. *Climate Dyn.*, **32 (2-3)**, 313–332.

Dunion, J. P., and C. S. Velden, 2004: The impact of the Saharan air layer on Atlantic tropical cyclone activity. *Bull. Amer. Meteor. Soc.*, **85 (3)**, 353–365.

Dunne, J. P., and Coauthors, 2012: GFDL's ESM2 Global Coupled Climate Carbon Earth System Models. Part I: Physical Formulation and Baseline Simulation Characteristics. *J. Climate*, **25 (19)**, 6646–6665, doi:10.1175/JCLI-D-11-00560.1.

Emanuel, K., and A. Sobel, 2013: Response of tropical sea surface temperature, precipitation, and tropical cyclone-related variables to changes in global and local forcing. *J. Adv. Model. Earth Syst.*, **5**, doi:10.1002/jame.20032.

Emanuel, K. A., 1986: An air-sea interaction theory for tropical cyclones. Part I: Steady-state maintenance. *J. Atmos. Sci.*, **43 (6)**, 585–605.

Emanuel, K. A., 1988: The maximum intensity of hurricanes. *J. Atmos. Sci.*, **45 (7)**, 1143–1155.

Evan, A. T., J. P. Kossin, V. Ramanathan, and Coauthors, 2011: Arabian Sea tropical cyclones intensified by emissions of black carbon and other aerosols. *Nature*, **479 (7371)**, 94–97.

Garner, S., 2015: The relationship between hurricane potential intensity and CAPE. *J. Atmos. Sci.*, **72 (1)**, 141–163.

GFDL Atmospheric Model Development Team, 2004: The new GFDL global atmosphere and land model AM2-LM2: Evaluation with prescribed SST simulations. *J. Climate*, **17 (24)**, 4641–4673.

Gilford, D. M., S. Solomon, and K. Emanuel, 2017: Radiative effects of stratospheric seasonal cycles in the tropical upper troposphere and lower stratosphere. *J. Climate*, **30 (8)**, 2769–2783.

Ginoux, P., J. M. Prospero, T. E. Gill, N. C. Hsu, and M. Zhao, 2012: Global-scale attribution of anthropogenic and natural dust sources and their emission rates based on MODIS Deep Blue aerosol products. *Rev. Geophys.*, **50 (3)**, RG3005.

Gray, W. M., 1998: The formation of tropical cyclones. *Meteor. Atmos. Phys.*, **67 (1-4)**, 37–69.

Grogan, D. F., T. R. Nathan, and S.-H. Chen, 2016: Effects of Saharan dust on the linear dynamics of African easterly waves. *J. Atmos. Sci.*, **73 (2)**, 891–911.

Guo, L., A. G. Turner, and E. J. Highwood, 2016: Local and remote impacts of aerosol species on Indian summer monsoon rainfall in a GCM. *J. Climate*, **29 (19)**, 6937–6955.

Haywood, J., and V. Ramaswamy, 1998: Global sensitivity studies of the direct radiative forcing due to anthropogenic sulfate and black carbon aerosols. *J. Geophys. Res.-Atmos.*, **103 (D6)**, 6043–6058.

Held, I. M., 2001: The partitioning of the poleward energy transport between the tropical ocean and atmosphere. *J. Atmos. Sci.*, **58 (8)**, 943–948.

Held, I. M., and B. J. Soden, 2006: Robust responses of the hydrological cycle to global warming. *J. Climate*, **19 (21)**, 5686–5699.

Held, I. M., and M. Zhao, 2011: The response of tropical cyclone statistics to an increase in CO_2 with fixed sea surface temperatures. *J. Climate*, **24 (20)**, 5353–5364.

Hill, S. A., Y. Ming, and M. Zhao, 2018: Robust responses of the Sahelian hydrological cycle to global warming. *J. Climate*.

Horowitz, L. W., 2006: Past, present, and future concentrations of tropospheric ozone and aerosols: Methodology, ozone evaluation, and sensitivity to aerosol wet removal. *J. Geophys. Res.-Atmos.*, **111**, D22211.

Horowitz, L. W., and Coauthors, 2003: A global simulation of tropospheric ozone and related tracers: Description and evaluation of MOZART, version 2. *J. Geophys. Res.-Atmos.*, **108 (D24)**, 4784.

Koch, D., and Coauthors, 2009: Evaluation of black carbon estimations in global aerosol models. *Atmos. Chem. Phys.*, **9**, 9001–9026.

Kovilakam, M., and S. Mahajan, 2016: Confronting the "Indian summer monsoon response to black carbon aerosol" with the uncertainty in its radiative forcing and beyond. *J. Geophys. Res.-Atmos.*, **121 (13)**, 7833–7852.

Lau, K., M. Kim, and K. Kim, 2006: Asian summer monsoon anomalies induced by aerosol direct forcing: the role of the Tibetan Plateau. *Climate Dyn.*, **26 (7-8)**, 855–864.

Lin, P., D. Paynter, Y. Ming, and V. Ramaswamy, 2017: Changes of the tropical tropopause layer under global warming. *J. Climate*, **30 (4)**, 1245–1258.

Mahajan, S., K. J. Evans, J. E. Truesdale, J. J. Hack, and J.-F. Lamarque, 2012: Interannual tropospheric aerosol variability in the late twentieth century and its impact on tropical Atlantic and West African climate by direct and semidirect effects. *J. Climate*, **25 (23)**, 8031–8056.

Mahmood, R., and S. Li, 2013: Delay in the onset of South Asian summer monsoon induced by local black carbon in an AGCM. *Theor. Appl. Climatol.*, **111 (3-4)**, 529–536.

Menon, S., J. Hansen, L. Nazarenko, and Y. Luo, 2002: Climate effects of black carbon aerosols in China and India. *Science*, **297 (5590)**, 2250–2253.

Miller, R., and I. Tegen, 1998: Climate response to soil dust aerosols. *J. Climate*, **11 (12)**, 3247–3267.

Ming, Y., and V. Ramaswamy, 2011: A model investigation of aerosol-induced changes in tropical circulation. *J. Climate*, **24 (19)**, 5125–5133.

Ming, Y., V. Ramaswamy, and G. Persad, 2010: Two opposing effects of absorbing aerosols on global-mean precipitation. *Geophys. Res. Lett.*, **37**, L13701.

Murakami, H., and Coauthors, 2012: Future changes in tropical cyclone activity projected by the new high-resolution MRI-AGCM. *J. Climate*, **25 (9)**, 3237–3260.

Myhre, G., and Coauthors, 2013: *Anthropogenic and Natural Radiative Forcing*, chap. 8, 659–740. Cambridge University Press, Cambridge, United Kingdom and New York, NY, USA, doi: 10.1017/CBO9781107415324.018.

Persad, G. G., Y. Ming, and V. Ramaswamy, 2012: Tropical tropospheric-only responses to absorbing aerosols. *J. Climate*, **25 (7)**, 2471–2480.

Persad, G. G., D. J. Paynter, Y. Ming, and V. Ramaswamy, 2017: Competing atmospheric and surface-driven impacts of absorbing aerosols on the East Asian summertime climate. *J. Climate*, **30 (22)**, 8929-8949.

Putman, W. M., and S.-J. Lin, 2007: Finite-volume transport on various cubed-sphere grids. *J. Comput. Phys.*, **227 (1)**, 55–78.

Rayner, N., D. E. Parker, E. Horton, C. Folland, L. Alexander, D. Rowell, E. Kent, and A. Kaplan, 2003: Global analyses of sea surface temperature, sea ice, and night marine air temperature since the late nineteenth century. *J. Geophys. Res.-Atmos.*, **108 (D14)**.

Sand, M., T. Iversen, P. Bohlinger, A. Kirkevåg, I. Seierstad, Ø. Seland, and A. Sorteberg, 2015: A standardized global climate model study showing unique properties for the climate response to black carbon aerosols. *J. Climate*, **28 (6)**, 2512–2526.

Shaevitz, D. A., and Coauthors, 2014: Characteristics of tropical cyclones in high-resolution models in the present climate. *J. Adv. Model. Earth. Sy.*, **6 (4)**, 1154–1172.

Sobel, A. H., J. Nilsson, and L. M. Polvani, 2001: The weak temperature gradient approximation and balanced tropical moisture waves. *J. Atmos. Sci.*, **58 (23)**, 3650–3665.

Strong, J. D., G. A. Vecchi, and P. Ginoux, 2015: The response of the tropical Atlantic and West African climate to Saharan dust in a fully coupled GCM. *J. Climate*, **28 (18)**, 7071–7092.

Sugi, M., H. Murakami, and J. Yoshimura, 2012: On the mechanism of tropical cyclone frequency changes due to global warming. *J. Meteor. Soc. Japan*, **90**, 397–408.

Twomey, S., 1974: Pollution and the planetary albedo. *Atmos. Environ.*, **8 (12)**, 1251–1256.

Walsh, K. J., and Coauthors, 2015: Hurricanes and climate: the US CLIVAR working group on hurricanes. *Bull. Amer. Meteor. Soc.*, **96 (6)**, 997–1017.

Wang, Y., K.-H. Lee, Y. Lin, M. Levy, and R. Zhang, 2014: Distinct effects of anthropogenic aerosols on tropical cyclones. *Nat. Clim. Change.*

Yoshimura, J., and M. Sugi, 2005: Tropical Cyclone Climatology in a High-resolution AGCM-Impacts of SST Warming and CO_2 Increase. *SOLA*, **1**, 133–136.

Yu, P., and Coauthors, 2017: Efficient transport of tropospheric aerosol into the stratosphere via the asian summer monsoon anticyclone. *Proc. Natl. Acad. Sci. (USA)*, **114 (27)**, 6972–6977.

Zhao, M., I. M. Held, and S.-J. Lin, 2012: Some counterintuitive dependencies of tropical cyclone frequency on parameters in a GCM. *J. Atmos. Sci.*, **69 (7)**, 2272–2283.

Zhao, M., I. M. Held, S.-J. Lin, and G. A. Vecchi, 2009: Simulations of global hurricane climatology, interannual variability, and response to global warming using a 50-km resolution GCM. *J. Climate*, **22 (24)**, 6653–6678.

LIST OF TABLES

TABLE 1. Tropical-mean changes in the various components of the atmospheric energy balance (W m^{-2}). The fractional changes (percentage) are in parentheses.

	δAS	δAL	δSH	δLH	$\delta(SH+LH)$
10X	9.9	-3.0	-2.5 (-11.9)	-4.2 (-4.5)	-6.7 (-5.9)
LAND	4.6	-1.6	-1.8 (-8.7)	-1.3 (-1.4)	-3.2 (-2.8)
OCEAN	5.2	-1.4	-0.76 (-3.6)	-2.9 (-3.2)	-3.7 (-3.2)
FT	5.2	-2.1	-0.77 (-3.6)	-2.2 (-2.4)	-3.0 (-2.6)
BL	5.0	-0.96	-1.9 (-8.9)	-2.1 (-2.2)	-4.0 (-3.5)
CO2	0.74	2.30	-0.59 (-2.8)	-2.4 (-2.6)	-3.0 (-2.6)

TABLE 2. Fractional changes (percentage) in TC and hurricane counts in the entire, Northern Hemisphere (NH) and Southern Hemisphere (SH) tropics. Statistically significant values are in bold.

	TC (Tropics)	TC (NH)	TC (SH)	Hurricane (Tropics)	Hurricane (NH)	Hurricane (SH)
10X	**-21**	**-17**	**-28**	**-26**	**-23**	**-34**
LAND	**-8.4**	**-7.2**	**-11**	**-15**	**-15**	**-13**
OCEAN	**-13**	-3.6	**-32**	**-14**	-5.1	**-39**
FT	**-14**	**-10**	**-23**	**-18**	**-15**	**-25**
BL	-1.6	1.7	**-8.7**	-3.8	-1.8	-9.1
CO2	**-9.4**	**-5.5**	**-18**	**-9.2**	**-8**	**-13**

TABLE 3. Fractional changes (percentage) of genesis-weighted precipitation (P), 500-hPa vertical velocity ($-\omega_{500}$), wind shear (S), potential intensity ($\mathscr{I}$), thermodynamic efficiency ($\mathscr{T}$) and enthalpy difference ($\mathscr{E}$).

	$\delta[P]_G$	$\delta[-\omega_{500}]_G$	$\delta[S]_G$	$\delta[\mathscr{I}]_G$	$\delta[\mathscr{T}]_G$	$\delta[\mathscr{E}]_G$
10X	-12	-19	4.6	-3.4	-2.4	-4.1
LAND	-5.6	-11	2.2	-1.1	-0.93	-0.93
OCEAN	-8.2	-11	2.7	-2.1	-1.5	-2.9
FT	-7.4	-13	2.9	-2.5	-2.1	-2.4
BL	-6.1	-8.0	2.3	-0.87	-0.38	-1.6
CO2	-5.5	-7.6	2.1	-1.5	-0.68	-2.5

LIST OF FIGURES

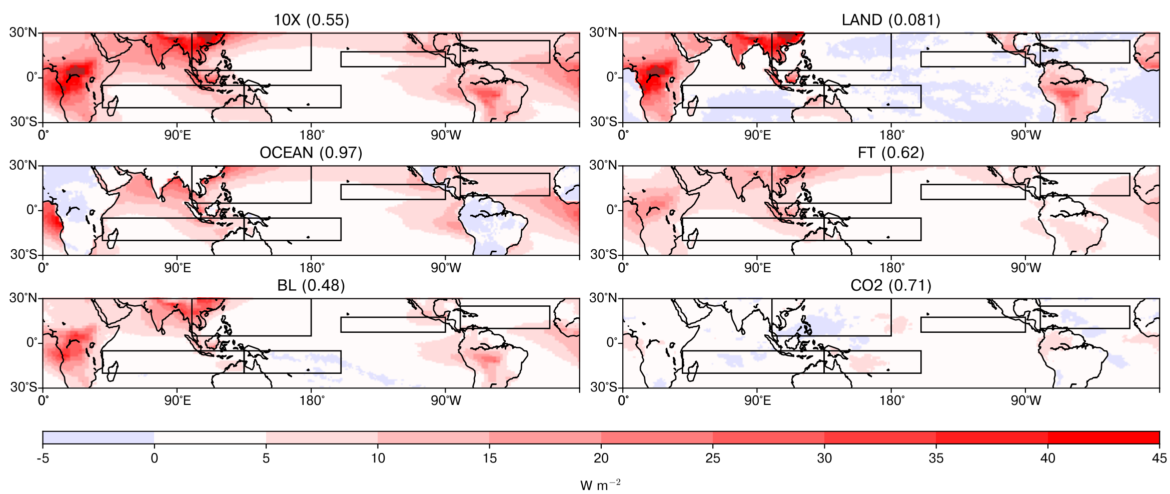

FIG. 1. Geographical distributions of the changes in atmospheric absorption (W m^{-2}, δAS (shortwave absorption) for BC cases and δAL (longwave absorption) for CO2). The numbers in parentheses indicate the fraction over the ocean (f_o). The rectangle boxes denotes the main development regions, as is the case for the other maps in this paper.

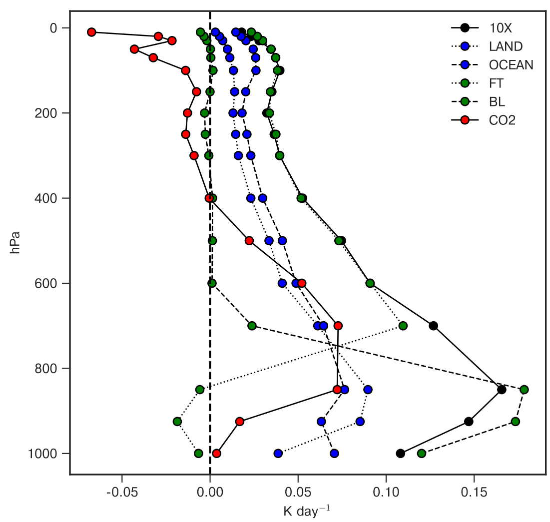

651 FIG. 2. Vertical distributions of the tropical-mean changes in radiative heating rate (K day^{-1}, shortwave for
652 the BC cases and longwave for CO2).

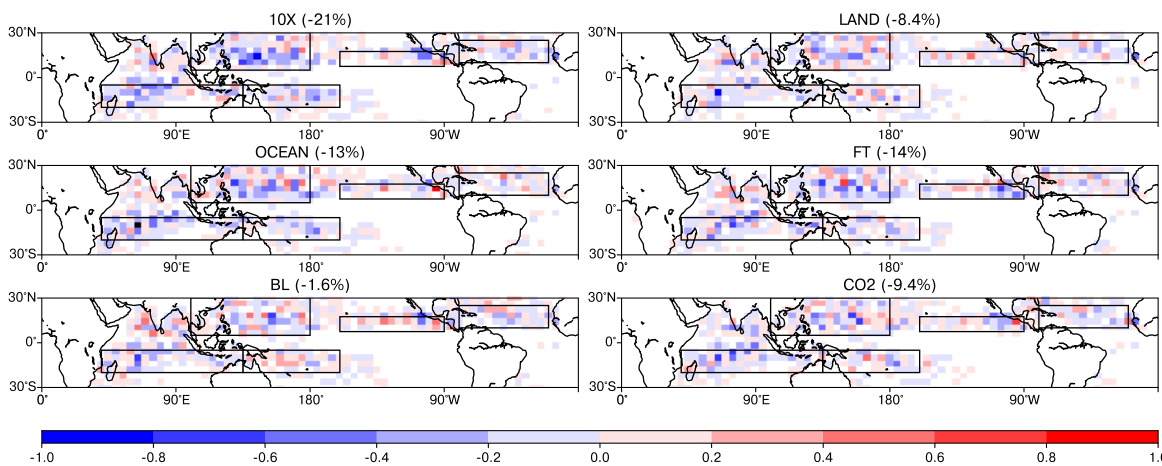

FIG. 3. Geographical distributions of the changes in annual-mean TC genesis counts averaged over 4° × 5° grids.

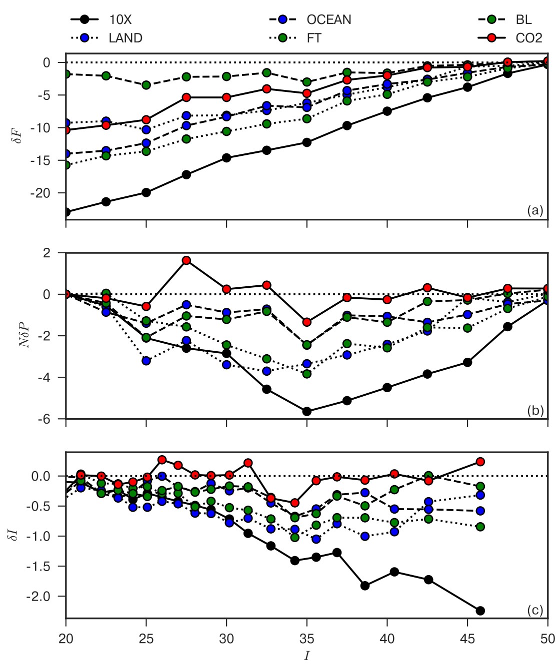

FIG. 4. Changes in TC intensity as measured by δF (upper), $N\delta P$ (middle) and δI (lower). See text for explanation.

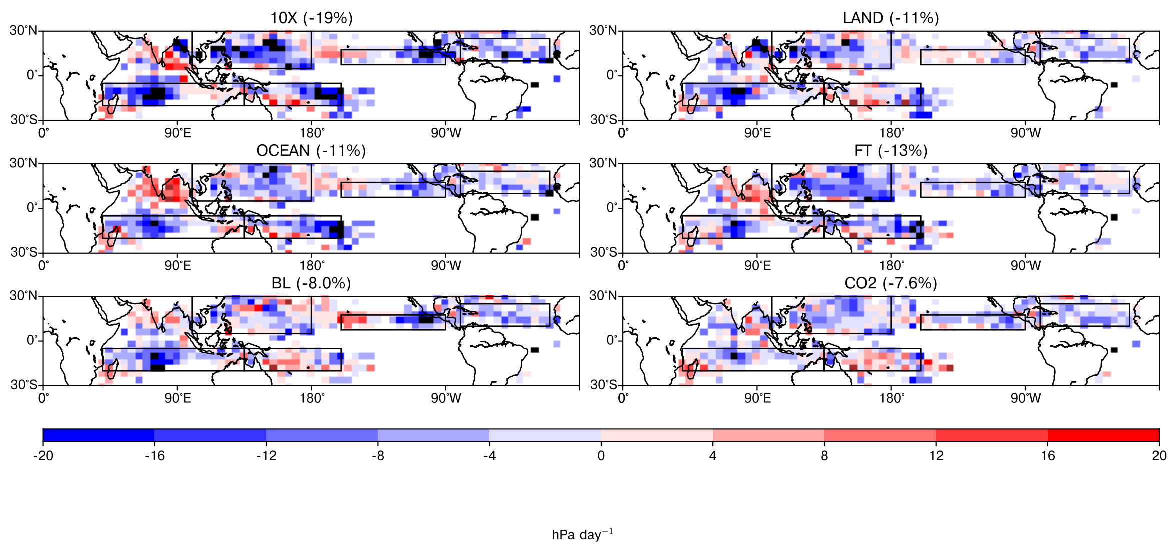

657 FIG. 5. Geographical distributions of the changes in genesis-weighted 500-hPa vertical velocity ($\delta[-\omega_{500}]_G$).
658 Tropical-mean values are in parentheses.

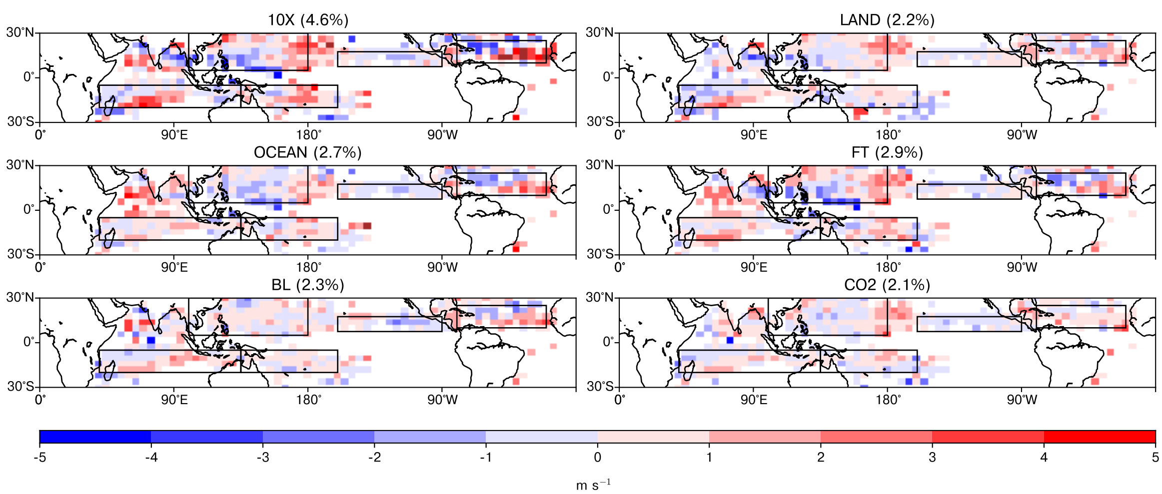

FIG. 6. Same as Figure 5, but for wind shear (S).

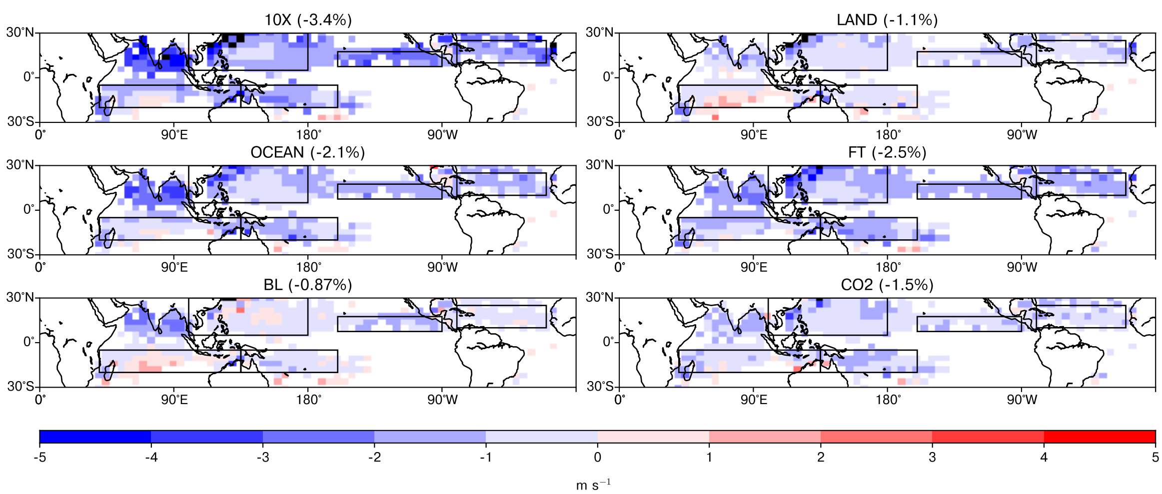

FIG. 7. Same as Figure 5, but for potential intensity ($\mathscr{I}$).

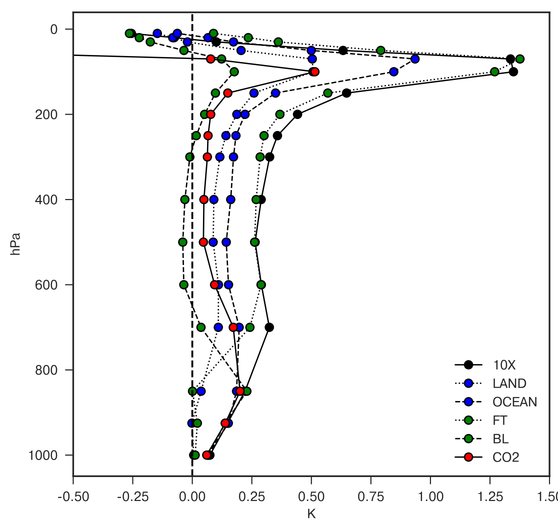

FIG. 8. Vertical distributions of the tropical-mean changes in air temperature (K).

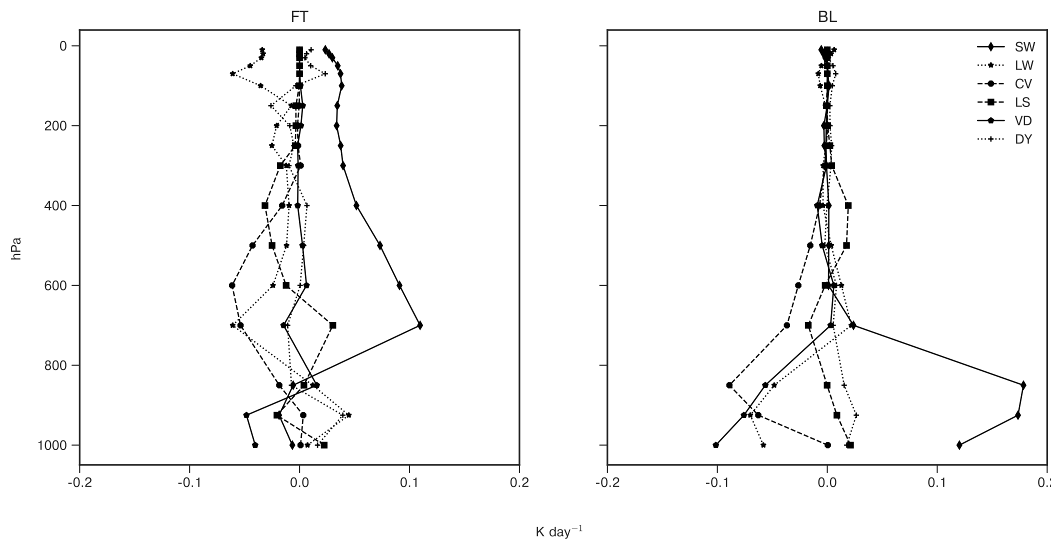

FIG. 9. Tropical-mean changes in atmospheric heating rates (K day^{-1}) in FT and BL. They include shortwave radiation (SW), longwave radiation (LW), convective (CV) and large-scale (LS) latent heating, and vertical diffusion (VD) and dynamical advection (DY) of sensible heat.